

000
001
002
003
004
005
006
007
008
009
010
011
012
013
014
015
016
017
018
019
020
021
022
023
024
025
026
027
028
029
030
031
032
033
034
035
036
037
038
039
040
041
042
043
044
045
046
047
048
049
050
051
052
053

Graph-Based Neural Reconstruction from Skeletonized 3D Networks

Anonymous CVPR submission

Paper ID 0446

Abstract

Advancements in electron microscopy image acquisition have created massive connectomics datasets in the terabyte range that make manual reconstruction of neuronal structures infeasible. Current state-of-the-art automatic methods segment neural membranes at the pixel level followed by agglomeration methods to create full neuron reconstructions. However, these approaches widely neglect global geometric properties that are inherent in the graph structure of neural wiring diagrams. In this work, we follow bottom-up pixel-based reconstruction by a top-down graph-based method to more accurately approximate neural pathways. We first generate skeletons in 3D from the membrane labels of the pixel-based segmentation. We then simplify this skeletonized 3D network into a 3D graph with nodes corresponding to labels from the segmentation and edges identifying potential locations of segmentation errors. We use a CNN classifier trained on ground truth data to generate edge weights on the 3D graph corresponding to error probabilities. We then apply a multicut algorithm to generate a partition on the graph that improves the final segmentation. Because the 3D graph is small and encodes top-down information our method is efficient and globally improves the neural reconstruction. We demonstrate the performance of our approach on multiple real-world connectomics datasets with an average variation of information improvement of $X \times$.

1. Introduction

The field of connectomics is concerned with reconstructing the wiring diagram of the brain at nanometer resolutions to enable new insights into the workings of the brain [8, 18]. Recent advancements in image acquisition using multi-beam serial-section electron microscopy (sSEM) have allowed researchers to produce

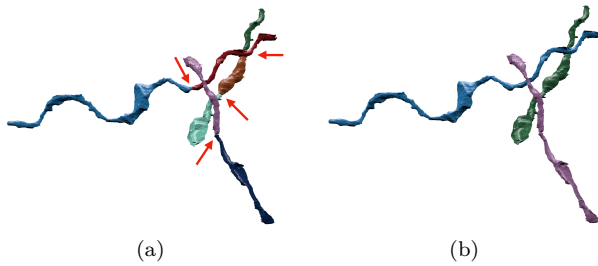


Figure 1: Example improvement of neural reconstruction. (a) We extract 3D skeletons from pixel-based segmentation algorithms to create a 3D graph representation. Edges with high segmentation error probabilities are indicated by the red arrows. (b) We improve the accuracy of segmentation using a graph partitioning algorithm, leveraging both local and global information.

terabytes of image data every hour [12]. It is not feasible for domain experts to manually reconstruct this vast amount of image data [11]. State-of-the-art automatic reconstruction approaches use pixel-based segmentation with convolutional neural networks (CNNs) followed by agglomeration strategies [21, 23, 27, 30, 33, 43]. These bottom-up pixel-based methods produce excellent results but still fall short of acceptable error rates for large volumes.

We present a top-down graph-based method that builds on the outputs of bottom-up pixel-based segmentation approaches. We first extract 3D skeleton networks from the input segmentation and generate a simplified 3D graph (Fig. 1a). We train a CNN classifier on the agglomerated regions in the segmentation data to detect errors. We run the classifier to populate the graph edge weights with error probabilities. We then use a graph optimization algorithm to partition the graph into the final improved reconstruction by enforcing domain-specific global constraints from biology (Fig. 1b).

054
055
056
057
058
059
060
061
062
063
064
065
066
067
068
069
070
071
072
073
074
075
076
077
078
079
080
081
082
083
084
085
086
087
088
089
090
091
092
093
094
095
096
097
098
099
100
101
102
103
104
105
106
107

108 Our approach operates at a level of abstraction
 109 above existing pixel-based methods. This allows us
 110 to leverage both local and global information to pro-
 111 duce more accurate reconstructions. Our method is
 112 independent of image resolution and acquisition pa-
 113 rameters, enabling its application to isotropic and
 114 anisotropic image data without retraining. Using the
 115 3D graph induced by the segmentation allows us to
 116 enforce global biological constraints on the reconstruc-
 117 tion. Our dual approach of assessing local decisions
 118 in a global context yields accuracy improvements over
 119 existing reconstruction methods.
 120

This work makes the following contributions: (1) a novel top-down method using graphs from skeletonized 3D networks for improved neural reconstruction of connectomics data; (2) a region-based CNN classifier to detect errors using the 3D graph as global constraint; (3) an empirical evaluation of our method on several connectomics datasets; (4) our method yields improved performance over a state-of-the-art pixel-based reconstruction approach on average by X percent without drastically increasing the running time.

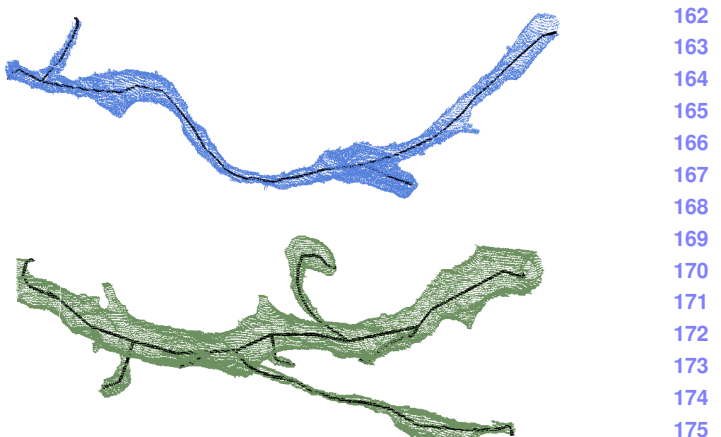
2. Related Work

We review some of the most successful segmentation methods that have been applied to large-scale EM images in connectomics.

Pixel-based methods. A large amount of connectomics research considers the problem of extracting segmentation information at the pixel (i.e., voxel) level from the raw EM images. Some early techniques apply computationally expensive graph partitioning algorithms with a single node per pixel [1]. However, these methods do not scale to terabyte datasets. More recent methods train classifiers to predict membrane probabilities per image slice either using 2D [4, 14, 19, 21, 41] or 3D CNNs [23, 33, 40].

Oftentimes these networks produce probabilities for the affinity between two voxels (i.e., the probability that adjacent voxels belong to the same neuron). The MALIS cost function is specifically designed for generating affinities that produce good segmentations [2]. More recently, flood-filling networks produce segmentations by training an end-to-end neural network that goes from EM images directly to label volumes [16]. These networks produce impressive accuracies but at a high computational cost.

Region-based methods. Several pixel-based approaches generate probabilities that neighboring pixels belong to the same neuron. Often a watershed



162
 163
 164
 165
 166
 167
 168
 169
 170
 171
 172
 173
 174
 175
 176
 177
 178
 179
 180
 181
 182
 183
 184
 185
 186
 187
 188
 189
 190
 191
 192
 193
 194
 195
 196
 197
 198
 199
 200
 201
 202
 203
 204
 205
 206
 207
 208
 209
 210
 211
 212
 213
 214
 215

Figure 2: Example skeletons (in black) extracted from segments (blue and green) using the TEASER algorithm.

algorithm will then cluster pixels into super-pixels [43]. Many methods build on top of these region-based strategies and train random-forest classifiers to produce the final segmentations [21, 27, 29, 30, 43].

Error-correction methods. Some recent research builds on top of these region-based methods to correct errors in the segmentation either using human proofreading [15, 22, 10, 9] or fully automatically [32, 44]. However, to our knowledge, our method is the first to extract a 3D graph from pixel-based segmentations for a true top-down error correction approach. This allows us to enforce domain-specific biology constraints and efficient graph partitioning algorithms. Many segmentation and clustering algorithms use graph partitioning techniques [1] or normalized cuts for traditional image segmentation [17, 36, 38]. Even though graph partitioning is an NP-Hard problem [5] there are several useful multicut heuristics that provide good approximations with reasonable computational costs [13]. We use the method of Keuper et al. [20] to partition the extracted 3D graph into the final neural reconstruction.

3. Method

There are two types of errors that can occur in connectomics segmentation. The first, called a split error, occurs when there are two segments that should have been merged. The second, called a merge error, happens when one segment should be split into two. Generally, it is much more difficult to correct merge errors than to correct split errors, as the space of possible split proposals grow quickly [28]. Thus, most reconstruction

216 approaches are tuned towards over-segmentation with
 217 many more split than merge errors. Our method takes
 218 as input over-segmentations of EM image volumes gen-
 219 erated by state-of-the-art connectomics reconstruc-
 220 tion pipelines (Sec. 4.2). Our goal is to identify loca-
 221 tions of split errors and merge the corresponding seg-
 222 ments automatically.
 223

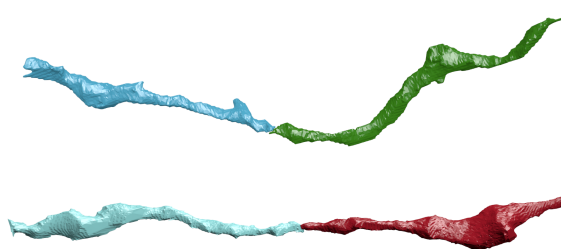
224 From the input segmentation we generate a graph
 225 G with nodes N and edges E with non-negative edge
 226 weights w_e . The nodes correspond to label segments
 227 from the segmentation with edges between segments
 228 considered for merging. Ideally, our graph has edges
 229 corresponding to all of the segments that were erro-
 230 neously split. To compute this graph we generate a
 231 skeleton for every segment in the pixel-based segmen-
 232 tation. The skeletonized 3D network is a simplified
 233 representation of the overall branching structure of the
 234 neurons. From these skeletons we identify potential
 235 merge locations and produce the corresponding edges
 236 for the graph. To find actual merges we run a classi-
 237 fication CNN to generate edge weights corresponding to
 238 merge probabilities. We then use a multicut algorithm
 239 to generate a partition on the graph where nodes in the
 240 same partition are assigned the same output label in
 241 the improved segmentation. We will now discuss the
 242 three major components to our framework (graph cre-
 243 ation, edge weights assignment, and graph partitioning)
 244 in more detail.

245 3.1. Node Generation

246 The simplest node generation strategy creates one
 247 node for every unique segment label in the input vol-
 248 ume. However, some of the millions of labels in the
 249 volume correspond to very small structures that are
 250 likely the result of segmentation errors, typically in
 251 regions with noisy raw image data. It is difficult to
 252 extract useful shape features from these segments be-
 253 cause of their small, often random, shape. We prune these
 254 nodes from the graph by removing all segments with
 255 fewer than a threshold $t_{seg} = 20,000$ voxels. This re-
 256 moved on average 56% of the segments in our datasets
 257 (Sec. 4.1). Despite the large number of segments, these
 258 regions only take up 1.6% of the total volume on aver-
 259 age.
 260

261 3.2. Edge Generation

262 A typical approach to generating edges produces an
 263 edge between all adjacent segments. Two segments l_1
 264 and l_2 are considered adjacent if there is a pair of adj-
 265 acent voxels with one labeled l_1 and the other labeled l_2 .
 266 For example, pixel-based agglomeration methods such
 267 as NeuroProof [29] and GALA [27] consider all pairs of
 268 adjacent segments for merging. However, this method
 269



270 Figure 3: Two erroneously split segments.
 271
 272
 273
 274
 275
 276
 277
 278
 279
 280
 281
 282
 283
 284
 285
 286
 287
 288
 289
 290
 291
 292
 293
 294
 295
 296
 297
 298
 299
 300
 301
 302
 303
 304
 305
 306
 307
 308
 309
 310
 311
 312
 313
 314
 315
 316
 317
 318
 319
 320
 321
 322
 323

283 produces too many edges in the graph for graph-based
 284 optimization approaches. We identify a smaller num-
 285 ber of pairs of segments to consider as graph edges
 286 using the following approach.
 287

288 First, we extract a skeleton from each segment in the
 289 label volume using the TEASER algorithm [34, 42].
 290 Fig. 2 shows an example of two extracted skeletons
 291 (in black). These skeletons consist of a sequence of
 292 joints, i.e., locations that are locally a maximum dis-
 293 tance from the segment boundary, with line segments
 294 connecting successive joints. We prune the joints that
 295 are within $t_{jnt} = 50$ voxels of each other to reduce un-
 296 necessary branching. We refer to joints that have only
 297 one connected neighbor as endpoints. Many of the seg-
 298 ments that are erroneously split have nearby endpoints
 299 (Fig. 3). We make use of this fact to merge segments
 300 with the following two-pass pruning algorithm.
 301

302 In the first pass, we iterate over all endpoints e be-
 303 longing to a segment S and create a set of segments
 304 \mathbb{S}'_e that includes all labels that are within t_{low} voxels
 305 from e . Elements of \mathbb{S}'_e are candidates for merging.
 306 However, this first pass often leads to too many can-
 307 didates, requiring an additional pass for further prun-
 308 ing. In the second pass, we consider all of the segments in
 309 \mathbb{S}'_e for every endpoint e . If a segment $S' \in \mathbb{S}'_e$ has an
 310 endpoint within t_{high} voxels of e , the segment S and
 311 S' are considered for merging. We store the midpoints
 312 between the two endpoints as the center of the poten-
 313 tial merges in the set \mathbb{S}_c . **HP: add how the final graph**
 314 **is constructed**

315 3.3. Edge Weights Assignment

316 We assign non-negative edge weights w_e to each edge
 317 where the weight corresponds to the probability that
 318 two nodes belong to the same neuron. Instead of using
 319 handcrafted features to compute the similarity between
 320 adjacent nodes, we train a 3D CNN classifier to learn
 321 from the manually labeled oversegmentation input vol-
 322 ume (Sec. 4.1).
 323

324 3.3.1 Classifier Input 378

325 We extract a cubic region of interest (ROI) around each 379 endpoint e in \mathbb{S}_c as input to the CNN. The CNN receives 380 three input channels for every voxel in the ROI 381 around segments l_1 and l_2 . The input in all of the 382 channels is in the range $\{-0.5, 0.5\}$. The first channel is 383 0.5 only if the corresponding voxel has label l_1 . The 384 second channel is 0.5 only if the corresponding voxel has 385 label l_2 . The third channel is 0.5 if the corresponding 386 voxel is either l_1 or l_2 . 387

336 3.3.2 Network Architecture & Training 388

339 We use the CNN architecture by Chatfield et al. [3]. 340 It consists of three layers of double convolutions 341 followed by a max pooling step. The first max pooling 342 layer is anisotropic with pooling only in the x and y 343 dimensions. The output of this final pooling step is 344 flattened into a 1D vector that is input into two fully 345 connected layers. The final layer produces probabilities 346 with a sigmoid activation function [6]. All of the other 347 activation functions are LeakyReLU [24]. 348

For training we use a stochastic gradient descent 349 optimizer with Nesterov’s accelerated gradient [26]. We 350 employ dropouts of 0.2 after every pooling layer and 351 the first dense layer, and a dropout of 0.5 after the 352 final dense layer to prevent overfitting. We discuss all 353 other network parameters in Sec. 4.4. 354

355 3.4. Graph Partitioning 366

357 After constructing the 3D graph we apply graph partitioning 358 using multicut to compute the final segmentation. 359 Using top-down graph partitioning allows us to 360 apply biological constraints on the output. Neuroscien- 361 tists know that neuronal connectivity graphs in the 362 brain are acyclic (i.e., the graphs have a genus of zero). 363 We enforce this constraint by finding a multicut parti- 364 tion of the graph that generates a forest of nodes, i.e., 365 a set of trees where no segment has a cycle. To solve 366 this constraining multicut problem we use the method 367 by Keuper et al. [20] that produces a feasible solution 368 by greedy additive edge contraction. 369

370 4. Experimental Results 371

372 We evaluate our method on two connectomics 373 datasets and compare it to a state-of-the-art pixel- 374 based reconstruction method using the variation of 375 information (VI) metric. **HP:** depending on space we 376 can shorten this and put details into the supplemental 377 material

4.1. Datasets 378

We use the following two datasets for training and experimental evaluation.

Kasthuri. The Kasthuri dataset consists of scanning electron microscope images of the neocortex of a mouse brain [18]. This dataset is $5342 \times 3618 \times 338$ voxels in size. The resolution of the dataset is $3 \times 3 \times 30 \text{ nm}^3$ per voxel. We evaluate our methods using the left cylinder of this 3-cylinder dataset. We downsample the dataset in the x and y dimensions to give a final resolution of $6 \times 6 \times 30 \text{ nm}^3$ per voxel. We divide the dataset into two volumes (Vol. 1 and Vol. 2) along the x dimension where each volume is $8.0 \times 10.9 \times 10.1 \mu\text{m}^3$.

FlyEM. The FlyEM dataset comes from the mushroom body of a 5-day old adult male Drosophila fly imaged by a focused ion-beam milling scanning electron microscopy [37]. The mushroom body in this species is the major site of associative learning. The original dataset contains a $40 \times 50 \times 120 \mu\text{m}^3$ volume of which we use two cubes of size $10 \times 10 \times 10 \mu\text{m}^3$. The resolution of this dataset is $10 \times 10 \times 10 \text{ nm}^3$ or 1000 voxels in each dimension in each of the two volumes.

4.2. Pixel-Based Segmentations 404

The segmentation on the Kasthuri dataset was computed by agglomerating 3D supervoxels produced by the z-watershed algorithm from 3D affinity predictions [43]. A recent study by Funke et al. [35] demonstrated superior performance of such methods over existing ones on anisotropic data. We learn 3D affinities using MALIS loss with a U-net [39, 33]. We apply the z-watershed algorithm with suitable parameters to compute a 3D oversegmentation of the volume. The resulting 3D oversegmentation is then agglomerated using the technique of context-aware delayed agglomeration to generate the final segmentation [29]. We use this segmentation as our baseline for comparisons with our method.

For the FlyEM data we collected two $1000 \times 1000 \times 1000$ voxel ($10 \times 10 \times 10 \mu\text{m}^3$) volumes from the authors [37]. Based on the authors’ suggestion, we applied a context-aware delayed agglomeration algorithm [29] that shows improved performance on this dataset over the pipeline used in the original publication. This segmentation framework learns voxel and supervoxel classifiers with an emphasis to minimize under-segmentation error. At the same time this framework produces lower oversegmentation than standard algorithms. The algorithm first computes multi-channel 3-D predictions for membranes, cell interiors,

and mitochondria, among other cell features. The membrane prediction channel is used to produce an over-segmented volume using 3D watershed, which is then agglomerated hierarchically up to a certain confidence threshold. We used exactly the same parameters as the publicly available code for this algorithm.

4.3. Graph Generation Parameters

There are two essential parameters to the graph generation algorithm described in Section 3.1: t_{low} and t_{high} . Ideally, the merge candidates output by this algorithm will contain all possible positive examples with a very limited number of negative examples. After considering various thresholds, we find that $t_{low} = 240\text{ nm}$ and $t_{high} = 600\text{ nm}$ produce the best results considering this objective.

In our implementation we use nanometers for these thresholds and not voxels. Connectomics datasets often have lower sample resolutions in z . Using nanometers allows us to have uniform units across all of these datasets and calculate the thresholds in voxels at runtime. For example, the thresholds in voxels are $t_{low} = (40, 40, 8)$ and $t_{high} = (100, 100, 20)$ for the anisotropic Kasthuri dataset and $t_{low} = (24, 24, 24)$ and $t_{high} = (60, 60, 60)$ for the isotropic FlyEM dataset.

4.4. Classifier Training

We use the left cylinder of the Kasthuri dataset for training and validation. We train on 80% of the potential merge candidates for this volume. We validate the CNN classifier on the remaining 20% of candidates. We apply data augmentation to the generated examples to increase the size of the training datasets. We consider all rotations of 90 degrees along the xy -plane in addition to mirroring along the x and z axes. This produces 16 times more training data.

We consider networks with varying input sizes, optimizers, loss functions, filter sizes, learning rates, and activation functions. The supplemental material includes information on the experiments that determined these final parameters. Table 1 provides the parameters of the final network. There are 7,294,705 learnable parameters in our final architecture. All the parameters are randomly initialized following the Xavier uniform distribution [7]. Training concluded after 34 epochs.

5. Results

5.1. Error Metric

We evaluate the performance of the different methods using the split version of variance of information (VI) [25]. Given a ground truth labeling GT

Parameters	Values	486
Loss Function	Mean Squared Error	487
Optimizer	SGD with Nesterov Momentum	488
Momentum	0.9	489
Initial Learning Rate	0.01	490
Decay Rate	$5 * 10^{-8}$	491
Activation	LeakyReLU ($\alpha = 0.001$)	492
Kernel Sizes	$3 \times 3 \times 3$	493
Filter Sizes	$16 \rightarrow 32 \rightarrow 64$	494

Table 1: Training parameters.

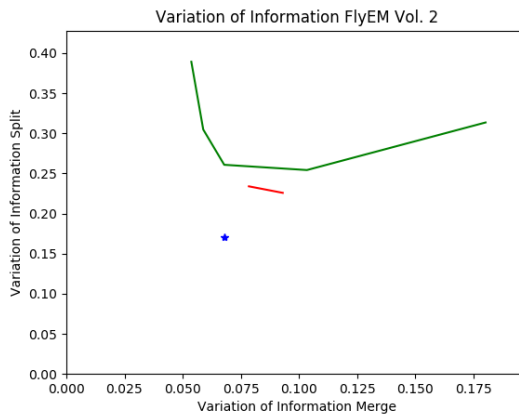
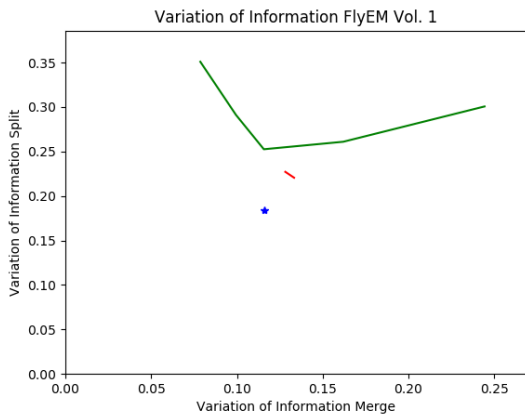
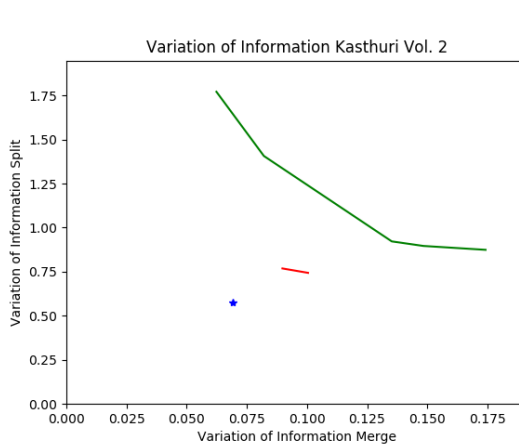
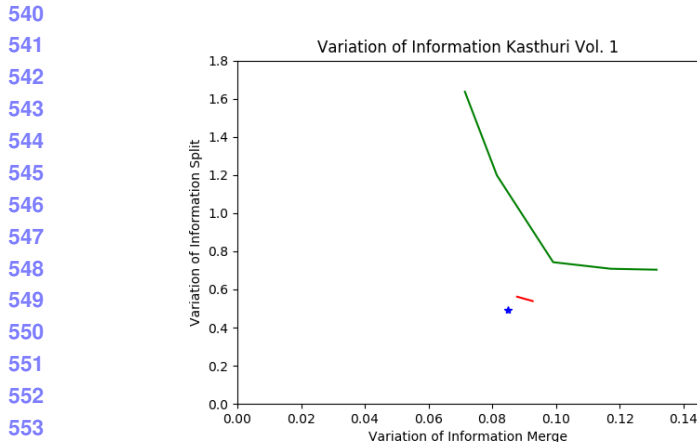
and our automatically reconstructed segmentation SG , over and undersegmentation are quantified by the conditional entropy $H(GT|SG)$ and $H(SG|GT)$, respectively. Since we are measuring the entropy between two clusterings, better VI scores are closer to the origin.

5.2. Variation of Information Improvement

In Fig. 4, we show the VI results of NeuroProof on the Kasthuri and FlyEM data at varying thresholds of agglomeration (green). The green circle represents the variation of information for our input segmentation (a threshold of 0.3 for all datasets). Our results are in red. We show the comparison to an oracle (blue) that correctly partitions the graph from our algorithm based on ground truth.

Our algorithm improves the accuracy of the input segmentation on every dataset, reducing the VI split score on average by X% and only increasing the VI merge score by X%. Scores closer to the origin are better for this metric, and in every instance we are below the green curve. We see significant improvements on the Kasthuri datasets (VI split reduction of X% and X% on the training and testing datasets respectively) and slightly more modest improvements on the FlyEM datasets (reduction of X% and X%). However, our baseline, NeuroProof performs much better on the FlyEM datasets reducing the potential improvement. Isotropic datasets are easier to segment using state-of-the-art region-based methods than anisotropic ones [31]. Thus there is less room for improvement on these datasets.

Fig. 5 shows successful merges on the Kasthuri Vol. 2 dataset. Several of these examples combine multiple consecutive segments that span the volume. In the third example we correct the oversegmentation of a dendrite. Fig. 6 shows some failure cases. In two of these examples the algorithm correctly predicted several merges but made one error. In the third example a merge error in the initial segmentation propagated to our output. We now analyze how each major com-



568
569 Figure 4: VI scores of our method (red) compared to the baseline segmentation (green) and an oracle (blue) that
570 optimally partitions the graph based on ground truth.

578 Table 2: The results of our skeleton graph pruning
579 heuristic compared to the baseline segmentation.

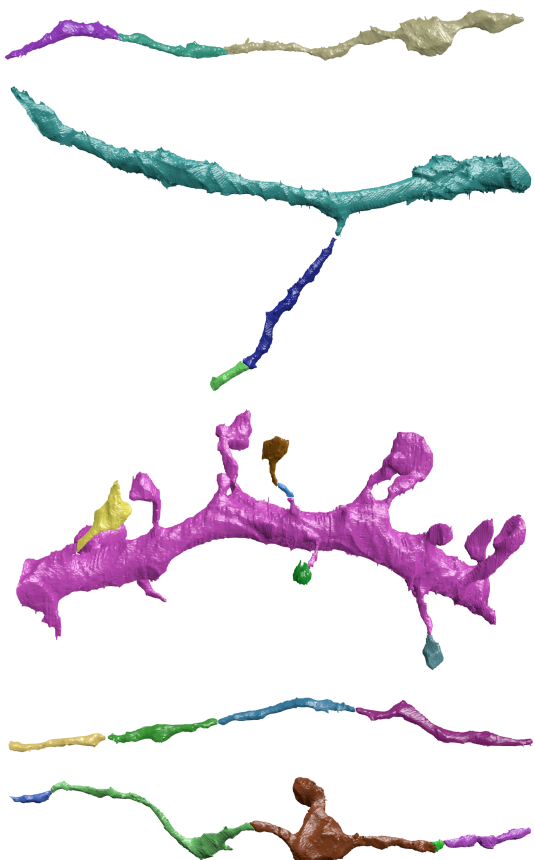
582 component of our method contributes to this final result.

5.3. Graph Creation

586 Table 2 shows the results of pruning the skeleton
587 graph using the heuristic discussed in Sec. 3.1. The
588 baseline algorithm considers all adjacent regions for
589 merging. Our method removes a significant portion
590 of these candidates while maintaining a large number
591 of the true merge locations. This edge pruning is essen-
592 tial for the graph partitioning algorithm, which has a
593 computational complexity dependence on the number

573 Dataset Baseline After Pruning
574 Kasthuri Vol. 1 763 / 21242 (3.47%) 753 / 3459 (17.88%)
575 Kasthuri Vol. 2 1010 / 26073 (3.73%) 904 / 4327 (17.28%)
576 FlyEM Vol. 1 269 / 14875 (1.78%) 262 / 946 (21.69%)
577 FlyEM Vol. 2 270 / 16808 (1.58%) 285 / 768 (27.07%)

623
624
625
626
627
628
629
630
631
632
633
634
635
636
637
638
639
640
641
642
643
644
645
646
647
Equally important is the number of split errors that
remain after pruning. These are the locations that we
want to merge to create a more accurate reconstruc-
tion. For every dataset, the number of true split errors
remains constant before and after pruning. However,
since our heuristic does not enforce an adjacency con-
straint of two regions when constructing edges in the
graph, the difference does not indicate the number of
examples excluded by pruning. In fact, our method
finds a number of examples that are non-adjacent. Fig-
ure 7 shows two example segments with split errors, one
that our algorithm missed (top) and one that it identi-
fied (bottom), despite the fact that the split segments
are not adjacent. Of the successful examples in Fig-
ure 5, the second and fourth groupings contain pairs of
non-adjacent segments that merge with our algorithm.



648
649
650
651
652
653
654
655
656
657
658
659
660
661
662
663
664
665
666
667
668
669
670
671
672
673
674
675
676
677
678
679
680
681
Figure 5: Correctly segmented neurons from our
method.

5.4. Classification Performance

682
683
684
685
686
687
688
689
690
691
692
693
694
695
696
697
698
699
700
701
Figure 8 shows the receiver operating characteristic (ROC) curve for all of the datasets. We train our CNN using one of the Kasthuri volumes and test using the other three datasets. Since our CNN only takes as input a region of the label volume we can train on an anisotropic dataset and infer on an isotropic one. This provides a major benefit given the time-intensive task of manually generating ground truth data at various resolutions.

As evidenced by the ROC curve, the test results on the Kasthuri data are better than the results for FlyEM. We believe this is in part because of the differences in the datasets (i.e., isotropy and xy resolution). To test this hypothesis, we also evaluate the performance of the FlyEM datasets when the network trains on FlyEM Vol. 1 and infers on FlyEM Vol. 2.¹ The

¹Since the FlyEM datasets have significantly fewer examples, we initialize the network with the weights from the Kasthuri training and have an initial learning rate of 10^{-4} .



702
703
704
705
706
707
708
709
710
711
712
713
714
715
716
717
718
719
720
721
722
723
724
725
726
727
728
729
730
731
732
733
734
735
736
737
738
739
740
741
742
743
744
745
746
747
748
749
750
751
752
753
754
755
Figure 6: Errors made by our method.



731
732
733
734
735
736
737
738
739
740
741
742
743
744
745
746
747
748
749
750
751
752
753
754
755
Figure 7: Example merge candidates.

dotted lines in the figure represent these tests. There is a slight performance increase for FlyEM Vol. 2. However, the FlyEM datasets have reasonable results when the network is trained by the Kasthuri data, and the results outside of this section follow from that setup.

5.5. Graph Based Strategies

The graph-based optimization strategy increases our correction accuracy over using just the CNN. In particular, the precision increases on each dataset, although the recall decreases on all but one of the datasets. Since it is more difficult to correct merge errors than split errors, it is often desirable to sacrifice recall for precision. Table 3 shows the changes in precision, recall, and accuracy for all four datasets compared to the CNN. Over the three testing datasets, applying a graph-based par-

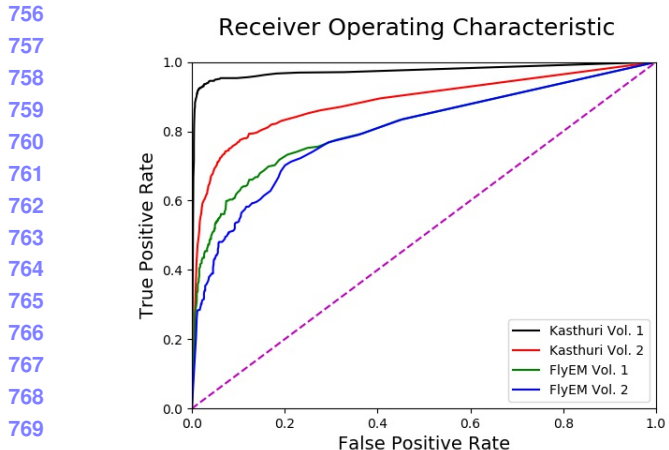


Figure 8: The receiver operating characteristic for all four datasets.

titioning strategy reduced the number of merge errors by X, Y, and Z.

Dataset	Δ Precision	Δ Recall	Δ Accuracy
Kasthuri Training	+3.60%	-0.01%	+0.60%
Kasthuri Testing	+7.59%	-1.77%	+1.38%
FlyEM Vol. 1	+2.68%	+0.76%	+0.66%
FlyEM Vol. 2	+2.22%	-1.05%	+0.29%

Table 3: Precision and recall for the training and three test datasets.

6. Conclusions

We present a novel method for reconstructing neuronal processes in connectomics datasets. We extend existing region-based reconstruction strategies using a morphological 3D skeleton graph and show significant accuracy improvement on two datasets from two different species. Our approach enables enforcing domain-constraints on the resulting segmentation. We believe this approach extends beyond connectomics to other domains with different constraints.

There is significant room for additional research related to this topic. We can still extract a lot more information from the skeletons of each segment. Currently these skeletons identify potential merge locations. However, these representations can be used to identify improperly merged segments. Additionally, we can further improve our results by tweaking the partitioning cost functions to more closely match the underlying biology. One such extension might take the outputs of a synaptic detector to enforce the constraint that a given segment only has post- or pre-synaptic connections.

References

- [1] B. Andres, T. Kroeger, K. L. Briggman, W. Denk, N. Korogod, G. Knott, U. Koethe, and F. A. Hama-precht. Globally optimal closed-surface segmentation for connectomics. In European Conference on Computer Vision, pages 778–791. Springer, 2012. 2
- [2] K. Briggman, W. Denk, S. Seung, M. N. Helmstaedter, and S. C. Turaga. Maximin affinity learning of image segmentation. In Advances in Neural Information Processing Systems, pages 1865–1873, 2009. 2
- [3] K. Chatfield, K. Simonyan, A. Vedaldi, and A. Zisserman. Return of the devil in the details: Delving deep into convolutional nets. arXiv preprint arXiv:1405.3531, 2014. 4
- [4] D. Ciresan, A. Giusti, L. M. Gambardella, and J. Schmidhuber. Deep neural networks segment neuronal membranes in electron microscopy images. In Advances in neural information processing systems, pages 2843–2851, 2012. 2
- [5] E. D. Demaine, D. Emanuel, A. Fiat, and N. Immorlica. Correlation clustering in general weighted graphs. Theoretical Computer Science, 361(2-3):172–187, 2006. 2
- [6] K.-I. Funahashi. On the approximate realization of continuous mappings by neural networks. Neural networks, 2(3):183–192, 1989. 4
- [7] X. Glorot and Y. Bengio. Understanding the difficulty of training deep feedforward neural networks. In Proceedings of the Thirteenth International Conference on Artificial Intelligence and Statistics, pages 249–256, 2010. 5
- [8] D. Haehn, J. Hoffer, B. Matejek, A. Suissa-Peleg, A. K. Al-Awami, L. Kamentsky, F. Gonda, E. Meng, W. Zhang, R. Schalek, et al. Scalable interactive visualization for connectomics. In Informatics, volume 4, page 29. Multidisciplinary Digital Publishing Institute, 2017. 1
- [9] D. Haehn, V. Kaynig, J. Tompkin, J. W. Lichtman, and H. Pfister. Guided proofreading of automatic segmentations for connectomics. arXiv preprint arXiv:1704.00848, 2017. 2
- [10] D. Haehn, S. Knowles-Barley, M. Roberts, J. Beyer, N. Kasthuri, J. Lichtman, and H. Pfister. Design and evaluation of interactive proofreading tools for connectomics. IEEE Transactions on Visualization and Computer Graphics (Proc. IEEE SciVis 2014), 20(12):2466–2475, 2014. 2
- [11] D. Haehn, S. Knowles-Barley, M. Roberts, J. Beyer, N. Kasthuri, J. W. Lichtman, and H. Pfister. Design and evaluation of interactive proofreading tools for connectomics. IEEE Transactions on Visualization and Computer Graphics, 20(12):2466–2475, 2014. 1
- [12] D. G. C. Hildebrand, M. Cicconet, R. M. Torres, W. Choi, T. M. Quan, J. Moon, A. W. Wetzel, A. S. Champion, B. J. Graham, O. Randlett, et al. Whole-brain serial-section electron microscopy in larval zebrafish. Nature, 545(7654):345–349, 2017. 1

- 864 [13] A. Horňáková, J.-H. Lange, and B. Andres. Analysis
865 and optimization of graph decompositions by lifted
866 multicuts. In International Conference on Machine
867 Learning, pages 1539–1548, 2017. 2
- 868 [14] V. Jain, B. Bollmann, M. Richardson, D. Berger,
869 M. Helmstädtter, K. Briggman, W. Denk, J. Bowden,
870 J. Mendenhall, W. Abraham, K. Harris, N. Kasthuri,
871 K. Hayworth, R. Schalek, J. Tapia, J. Lichtman, and
872 S. Seung. Boundary learning by optimization with
873 topological constraints. In Proc. IEEE CVPR 2010,
874 pages 2488–2495, 2010. 2
- 875 [15] Janelia Farm. Raveler. <https://openwiki.janelia.org/wiki/display/flyem/Raveler>, 2014. Accessed on
876 11/01/2016. 2
- 877 [16] M. Januszewski, J. Maitin-Shepard, P. Li, J. Kornfeld,
878 W. Denk, and V. Jain. Flood-filling networks. arXiv
879 preprint arXiv:1611.00421, 2016. 2
- 880 [17] J. H. Kappes, M. Speth, G. Reinelt, and C. Schnörr.
881 Higher-order segmentation via multicuts. Computer
882 Vision and Image Understanding, 143:104–119, 2016.
883 2
- 884 [18] N. Kasthuri, K. J. Hayworth, D. R. Berger, R. L.
885 Schalek, J. A. Conchello, S. Knowles-Barley, D. Lee,
886 A. Vázquez-Reina, V. Kaynig, T. R. Jones, et al. Sat-
887 urated reconstruction of a volume of neocortex. Cell,
888 162(3):648–661, 2015. 1, 4
- 889 [19] V. Kaynig, A. Vazquez-Reina, S. Knowles-Barley,
890 M. Roberts, T. R. Jones, N. Kasthuri, E. Miller,
891 J. Lichtman, and H. Pfister. Large-scale automatic
892 reconstruction of neuronal processes from electron mi-
893 croscopy images. Medical image analysis, 22(1):77–88,
894 2015. 2
- 895 [20] M. Keuper, E. Levinkov, N. Bonneel, G. Lavoué,
896 T. Brox, and B. Andres. Efficient decomposition of im-
897 age and mesh graphs by lifted multicuts. In Proceed-
898 ings of the IEEE International Conference on Com-
899 puter Vision, pages 1751–1759, 2015. 2, 4
- 900 [21] S. Knowles-Barley, V. Kaynig, T. R. Jones, A. Wil-
901 son, J. Morgan, D. Lee, D. Berger, N. Kasthuri,
902 J. W. Lichtman, and H. Pfister. Rhoananet pipeline:
903 Dense automatic neural annotation. arXiv preprint
904 arXiv:1611.06973, 2016. 1, 2
- 905 [22] S. Knowles-Barley, M. Roberts, N. Kasthuri, D. Lee,
906 H. Pfister, and J. W. Lichtman. Mojo 2.0: Connectome
907 annotation tool. Frontiers in Neuroinformatics, (60),
908 2013. 2
- 909 [23] K. Lee, A. Zlateski, V. Ashwin, and H. S. Seung. Re-
910 cursive training of 2d-3d convolutional networks for
911 neuronal boundary prediction. In Advances in Neu-
912 ral Information Processing Systems, pages 3573–3581,
913 2015. 1, 2
- 914 [24] A. L. Maas, A. Y. Hannun, and A. Y. Ng. Rectifier
915 nonlinearities improve neural network acoustic models.
916 In Proc. ICML, volume 30, 2013. 4
- 917 [25] M. Meila. Comparing clusterings by the variation of in-
formation. In *Colt*, volume 3, pages 173–187. Springer,
2003. 5
- 918 [26] Y. Nesterov. A method of solving a convex program-
919 ming problem with convergence rate $O(1/k^2)$. 4
- 920 [27] J. Nunez-Iglesias, R. Kennedy, S. M. Plaza,
921 A. Chakraborty, and W. T. Katz. Graph-based ac-
922 tive learning of agglomeration (gala): a python library
923 to segment 2d and 3d neuroimages. *Frontiers in neu-*
924 *roinformatics*, 8, 2014. 1, 2, 3
- 925 [28] T. Parag. What properties are desirable from an
926 electron microscopy segmentation algorithm. arXiv
927 preprint arXiv:1503.05430, 2015. 2
- 928 [29] T. Parag, A. Chakraborty, S. Plaza, and L. Scheff-
929 er. A context-aware delayed agglomeration framework
930 for electron microscopy segmentation. *PLOS ONE*,
931 10(5):1–19, 05 2015. 2, 3, 4
- 932 [30] T. Parag, F. Tschopp, W. Grisaitis, S. C. Turaga,
933 X. Zhang, B. Matejek, L. Kamentsky, J. W. Licht-
934 man, and H. Pfister. Anisotropic em segmentation by
935 3d affinity learning and agglomeration. arXiv preprint
936 arXiv:1707.08935, 2017. 1, 2
- 937 [31] S. M. Plaza, T. Parag, G. B. Huang, D. J. Olbris,
938 M. A. Saunders, and P. K. Rivlin. Annotating synapses
939 in large em datasets. arXiv preprint arXiv:1409.1801,
940 2014. 5
- 941 [32] D. Rolnick, Y. Meirovitch, T. Parag, H. Pfister,
942 V. Jain, J. W. Lichtman, E. S. Boyden, and N. Shavit.
943 Morphological error detection in 3d segmentations.
arXiv preprint arXiv:1705.10882, 2017. 2
- 944 [33] O. Ronneberger, P. Fischer, and T. Brox. U-net:
945 Convolutional networks for biomedical image segmen-
946 tation. In International Conference on Medical Im-
947 age Computing and Computer-Assisted Intervention,
948 pages 234–241. Springer, 2015. 1, 2, 4
- 949 [34] M. Sato, I. Bitter, M. A. Bender, A. E. Kaufman, and
950 M. Nakajima. Teasar: Tree-structure extraction algo-
951 rithm for accurate and robust skeletons. In Computer
952 Graphics and Applications, 2000. Proceedings. The
953 Eighth Pacific Conference on, pages 281–449. IEEE,
2000. 3
- 954 [35] P. Schlegel, M. Costa, and G. S. Jefferis. Learning from
955 connectomics on the fly. *Current Opinion in Insect
Science*, 2017. 4
- 956 [36] J. Shi and J. Malik. Normalized cuts and image seg-
957 mentation. *IEEE Transactions on pattern analysis and
machine intelligence*, 22(8):888–905, 2000. 2
- 958 [37] S.-y. Takemura, Y. Aso, T. Hige, A. M. Wong, Z. Lu,
959 C. S. Xu, P. K. Rivlin, H. F. Hess, T. Zhao, T. Parag,
960 S. Berg, G. Huang, W. T. Katz, D. J. Olbris, S. M.
961 Plaza, L. A. Umayam, R. Aniceto, L.-A. Chang,
962 S. Lauchie, and et al. A connectome of a learning and
963 memory center in the adult drosophila brain. *eLife*,
964 6:e26975, 2017 Jul 18 2017. 4
- 965 [38] S. Tatiraju and A. Mehta. Image segmentation using
966 k-means clustering, em and normalized cuts. Depart-
967 ment of EECS, 1:1–7, 2008. 2
- 968 [39] S. Turaga, K. Briggman, M. Helmstaedter, W. Denk,
969 and S. Seung. Maximin affinity learning of image seg-
970 mentation. In Advances in Neural Information Pro-
971 cessing Systems 22. 2009. 4

- 972 [40] S. C. Turaga, J. F. Murray, V. Jain, F. Roth, M. Helmstaedter, K. Briggman, W. Denk, and H. S. Seung.
973 Convolutional networks can learn to generate affinity
974 graphs for image segmentation. Neural computation,
975 22(2):511–538, 2010. 2
976
- 977 [41] A. Vázquez-Reina, M. Gelbart, D. Huang, J. Lichtman, E. Miller, and H. Pfister. Segmentation fusion
978 for connectomics. In Proc. IEEE ICCV, pages 177–
979 184, Nov 2011. 2
980
- 981 [42] T. Zhao and S. M. Plaza. Automatic neuron type
982 identification by neurite localization in the drosophila
983 medulla. arXiv preprint arXiv:1409.1892, 2014. 3
984
- 985 [43] A. Zlateski and H. S. Seung. Image segmentation by
986 size-dependent single linkage clustering of a watershed
987 basin graph. arXiv preprint arXiv:1505.00249, 2015.
988 1, 2, 4
989
- 990 [44] J. Zung, I. Tartavull, and H. S. Seung. An error
991 detection and correction framework for connectomics.
992 CoRR, abs/1708.02599, 2017. 2
993
- 994
- 995
- 996
- 997
- 998
- 999
- 1000
- 1001
- 1002
- 1003
- 1004
- 1005
- 1006
- 1007
- 1008
- 1009
- 1010
- 1011
- 1012
- 1013
- 1014
- 1015
- 1016
- 1017
- 1018
- 1019
- 1020
- 1021
- 1022
- 1023
- 1024
- 1025
- 1026
- 1027
- 1028
- 1029
- 1030
- 1031
- 1032
- 1033
- 1034
- 1035
- 1036
- 1037
- 1038
- 1039
- 1040
- 1041
- 1042
- 1043
- 1044
- 1045
- 1046
- 1047
- 1048
- 1049
- 1050
- 1051
- 1052
- 1053
- 1054
- 1055
- 1056
- 1057
- 1058
- 1059
- 1060
- 1061
- 1062
- 1063
- 1064
- 1065
- 1066
- 1067
- 1068
- 1069
- 1070
- 1071
- 1072
- 1073
- 1074
- 1075
- 1076
- 1077
- 1078
- 1079